Austenite carbon enrichment and decomposition during quenching and tempering of high silicon high carbon bearing steel

Ribamar, G. G.; Escobar, J. D.; Kwiatkowski da Silva, A.; Schell, N.; Ávila, J. A.; Nishikawa, A. S.; Oliveira, J. P.; Goldenstein, H.

DOI
10.1016/j.actamat.2023.118742

Publication date
2023

Document Version
Final published version

Published in
Acta Materialia

Acta Materialia 247 (2023) 118742

Contents lists available at ScienceDirect

Acta Materialia

journal homepage: www.elsevier.com/locate/actamat

Full length article

Austenite carbon enrichment and decomposition during quenching and tempering of high silicon high carbon bearing steel

G.G. Ribamar [a,*], J.D. Escobar [a], A. Kwiatkowski da Silva [b], N. Schell [c], J.A. Ávila [d,e], A.S. Nishikawa [f], J.P. Oliveira [g], H. Goldenstein [a]

[a] Department of Metallurgical and Materials Engineering, University of São Paulo, Av. Prof. Mello Moraes, 2463, 05508-030, São Paulo, Brazil
[b] Department of Microstructure Physics and Alloy Design, Max-Planck-Institut für Eisenforschung, Düsseldorf, Germany
[c] Institute of Materials Physics, Helmholtz-Zentrum Hereon, Max-Planck-Str. 1, Geesthacht d-21502, Germany
[d] Department of Strength of Materials and Structural Engineering, Barcelona School of Engineering (ETSEIB), Universitat Politècnica de Catalunya, Avda. Diagonal 647, 08028 Barcelona, Spain
[e] Campus of São João da Boa Vista, São Paulo State University (UNESP), 13876-750, São João da Boa Vista, São Paulo, Brazil
[f] Department of Materials Science and Engineering, Delft University of Technology, Mekelweg 2, Delft, 2628 CD, the Netherlands
[g] CENIMAT/I3N, Department of Materials Science, NOVA School of Science and Technology, Universidade NOVA de Lisboa, 2829-516 Caparica, Portugal

ARTICLE INFO

Keywords:
Carbon partitioning
Austenite stabilization
Synchrotron radiation
Quenching and tempering
Microstructure

ABSTRACT

The addition of Si to steels is a well stablished method to delay cementite precipitation, allowing for carbon partitioning from martensite to retained austenite during tempering. It has been argued that carbon enrichment and stabilization of austenite leads to increased ductility and toughness. This has been the main motivation for the development of novel heat treatments, such as quenching and partitioning. High carbon steels can also benefit from improved ductility provided by the presence of stabilized retained austenite. However, the process of carbon partitioning is less understood due to the increased tendency for competitive carbide formation with increasing carbon content. The present work investigates the austenite carbon partitioning and austenite decomposition phenomena in a modified 1.82 wt.% Si hypereutectoid bearing steel during tempering. Dilatometry, in-situ and ex-situ synchrotron X-ray diffraction, 3D atom probe tomography, scanning electron microscopy, and hardness measurements were used. The results are discussed based on different equilibrium states between α' and carbides. It was found that carbon partitioning towards retained austenite occurs for several minutes without significant phase decomposition at temperatures lower than 300 °C. A transition temperature between prevalent austenite carbon enrichment and austenite decomposition occurs at 350 °C. Secondary cementite precipitation inside martensite, and at the α'/γ interfaces, is observed during tempering at temperatures above 400 °C. Results from constrained carbon equilibrium modeling with carbide presence indicate that homogeneously dispersed spheroidized primary cementite has little influence in the carbon partitioning phenomenon.

1. Introduction

High carbon bearing steels (wt.% C > 0.8) are well-known for their excellent rolling contact fatigue and wear resistance, with simultaneous low toughness and ductility [1–6]. Typically, their microstructure consists of hard tempered martensite (α'_t) + spheroidized cementite (θ) + a small amount of retained austenite (γ_R), usually below 5% vol. This complex microstructure is achieved through quenching from an intercritical annealing (in the θ + γ phase field) followed by tempering at low temperature (200–250 °C) [7]. Among these steels, AISI 52100 is one of the most well-known low production cost high-carbon-bearing steels.

The target hardness of 60 HRC (≈ 700 HV) desired for bearing applications [1] compromises a fracture toughness in a range of 41–53 MPa.$\sqrt{m}$ and the impact toughness to a range of 43–74 J [8]. New heat treatments and alloy design strategies are currently being explored to address and improve the inherent brittleness of high carbon bearing steel microstructures [9–11]. However, this is a complex task which requires carefully designed tempering cycles to reduce hardness without compromising wear performance.

Speer et al. [12,13] proposed a heat treatment, currently known as

* Corresponding author.
E-mail address: giovanigoncalvesr@usp.br (G.G. Ribamar).

https://doi.org/10.1016/j.actamat.2023.118742
Received 14 September 2022; Received in revised form 2 January 2023; Accepted 1 February 2023
Available online 2 February 2023

quenching and partitioning (Q&P), that produces a complex microstructure comprised of martensite (α') and stabilized (or partially stabilized) austenite, γ_R. The improvement of ductility is related to significant work-hardening of γ_R and/or deformation-induced plasticity occurring during the γ_R to α' transformation [14,15]. Stabilization of γ_R is achieved via carbon partitioning and this process has been successfully demonstrated in low carbon [16–18], high carbon [19,20], and stainless [21] steels. Nevertheless, fundamental understanding of γ_R stabilization through Q&P or Q&T of high carbon steels has received much less attention [19,20,22].

The extent of γ_R stabilization (via Q&P or Q&T), strongly depends on the proper selection of partitioning/tempering times and temperatures. This is of paramount interest especially in high carbon steels due to the strong tendency of γ_R decomposition into carbides or bainite. Numerical modeling efforts from Santofimia et al. [23] indicate that carbon partitioning towards γ_R occurs within 10 s at 300 °C. According to Clark et al. [24], maximum carbon partitioning into γ_R occurs after 100 s at temperatures between 200 and 260 °C, while γ_R decomposition into bainite occurs after 1000 s. Results from Nishikawa et al. [25] indicate that carbon enrichment in γ_R is accelerated under the presence of bainite. Regarding carbide precipitation, the contributions from Toji et al. [20] and Pierce et al. [26], show that the formation of η phase limits the amount of carbon partitioning towards γ_R. However, results from Toji, Miyamoto, and Raabe [19] indicate that carbon enrichment of γ_R is still thermodynamically possible when cementite precipitates in martensite. Similarly, Nishikawa et al. [22] studied the influence of carbides with different Gibbs energies on the kinetics of the carbon redistribution in a ductile cast iron. Results indicate that higher partitioning temperatures (> 450 °C) enable the formation of more stable carbides (cementite), while less stable carbides are formed at lower temperatures between 300 and 375 °C. For higher tempering temperatures, the work from Ayenampudi et al. [27] shows carbon enrichment into γ_R during tempering at 450 °C for 3600 s. However, pearlite precipitation simultaneously occurs, decreasing the amount of stable γ_R. Finally, the work from Celada-Casero et al. indicates that the prior austenite grain size also has an effect on the γ_R carbon enrichment during partitioning [28], with smaller prior austenite grain sizes resulting in more efficient carbon partitioning process.

Regarding alloy design aspects, silicon and carbon contents play an important role in the kinetics of martensite and γ_R decomposition [23,29,30]. For example, the addition of approximately 1.4 wt.% Si to transformation-induced plasticity steels is useful to delay the precipitation of cementite [31], which in turn extends the thermal stability of γ_R during carbon partitioning [32]. Therefore, the main motivation of this work is to use a modified high silicon bearing steel to delay the precipitation of cementite, thus extending the effective time for carbon partitioning into γ_R. Such alloy modification coupled with in situ X-ray diffraction offers a unique opportunity to study the competitive phenomena of carbon partitioning and carbide precipitation as a function of time and temperature.

The present work uses advanced microstructural characterization and thermodynamic modeling to understand the process of carbon mobility during tempering of a Si-modified high carbon bearing steel. In situ synchrotron X-ray diffraction measurements were conducted to study the competitive phenomena of carbon partitioning into γ_R and secondary cementite precipitation at temperatures between 200 °C and 500 °C. Scanning electron microscopy (SEM) and microhardness were used to characterize the microstructural evolution after tempering. Atom probe tomography (APT) was used to quantify the carbon partitioning occurring within the stabilization (300 °C) and decomposition (400 °C) regimes for γ_R. Constrained carbon equilibrium with carbide presence (CCEθ) model was used to clarify the role of primary and secondary cementite on the composition of austenite at the tempering temperatures of interest.

2. Experimental methods

2.1. Material

A novel high-silicon high-carbon steel, based on commercial AISI 52100 (DIN 100Cr6) grade, is proposed in this study. Silicon was added to delay cementite formation, while the manganese content was increased to maintain the Acm temperature close to that of the original alloy. The nominal chemical composition is detailed in Table 1. A_1 and Acm were determined by CALPHAD method using the Thermo-Calc® software with TCFE9 database to be 752 °C and 910 °C, respectively. The material was austenitized at 865 °C in the γ + θ field for all heat treatment conditions. The equilibrium austenite and cementite volume percentages calculated at 865 °C are 97.1% and 2.9%, respectively. The austenite composition at the austenitization temperature (865 °C) is also depicted in Table 1.

2.2. Heat treatment cycles

Cylindrical samples with 10 mm in length and 4 mm in diameter were heat-treated in a modified Bähr DIL 805A dilatometer. The heating and isothermal stages were performed in a vacuum. Helium was used in the cooling stages at a controlled cooling rate of 30 °C/s. Before the tempering heat treatment cycles studied in this work, all samples were subjected to intercritical annealing at 865 °C (γ + θ field) for 30 min, followed by quenching to room temperature. As a result, a complex microstructure of fresh martensite + retained austenite + spheroidized cementite homogeneously distributed in the matrix was obtained. From this starting microstructure, two types of heat-treatment cycles starting from the as-quenched microstructure were carried out: (i) continuous heating, and (ii) isothermal tempering. In the type (i) cycle, shown in Fig. 1a, an exploratory continuous heating cycle was conducted at 0.833 °C.s^{-1} to determine the critical temperatures for tempering reactions. Type (ii) heat-treatments, shown in Fig. 1b, consisted of a fixed 30 min (1800s) isothermal soaking time at temperatures between 200 and 500 °C.

In-situ synchrotron X-ray diffraction (SXRD) was performed during continuous heating and isothermal tempering cycles, providing real-time crystallographic information, enabling the quantification of the volume fraction and lattice parameter of γ_R during all treatment steps. These experiments were carried out at the X-ray Scattering and Thermo-Mechanical Simulation (XTMS) beamline at the Brazilian Synchrotron Light Laboratory (LNLS), located at the Brazilian Center for Research in Energy and Materials (CNPEM). The XTMS facility consisted of an adapted Gleeble 3S50™ thermo-mechanical simulator machine integrated into a synchrotron monochromatic 12 keV X-ray beam (λ = 1.033 Å). The scattered X-ray intensities were collected using a Rayonix 2D detector, allowing the observation of partial diffraction rings in a reflection diffraction mode geometry. These rings were integrated to obtain 1D diffractograms. The XRD patterns were acquired with an exposure time of 5.9 s. The observed angular range comprised the peaks {111}γ, {110}α, {200}γ, and {200}α.

Additional high energy synchrotron X-ray diffraction (HEXRD) analysis was conducted to obtain high-resolution diffraction before and after the tempering cycles. Single-shot *ex situ* experiments were carried

Table 1
Steel global chemical composition (Steel) and its austenite chemical composition at 865 °C calculated using the CALPHAD method (γ – 865 °C). Data in wt.% (at. %).

	C	Mn	Cr	Si	Fe
Steel	0.99 (4.404)	1.00 (0.963)	1.50 (1.526)	1.82 (3.428)	Bal.
γ – 865 °C	0.834 (3.692)	0.987 (0.956)	1.266 (1.295)	1.873 (3.546)	Bal.

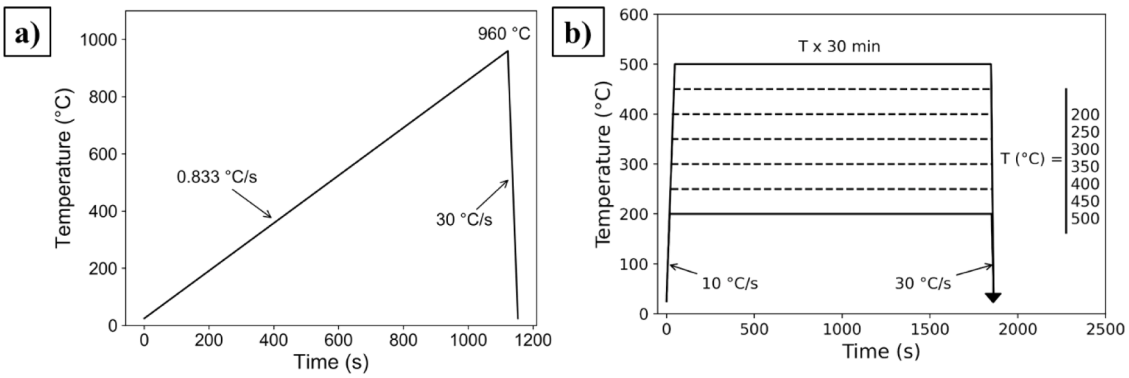

Fig. 1. Schematic representation of (a) continuous heating cycle; (b) tempering heat treatment cycles.

out at the P07 beamline at the German Electron Synchrotron (DESY), Hamburg, Germany. A monochromatic 87.1 keV X-ray beam (λ = 0.14235 Å) covering an area of 0.5 × 0.5 mm was used in transmission mode. Complete Debye-Scherrer rings were collected with a PerkinElmer fast detector, and then integrated along the full azimuthal angle using the free open software Fit2D to obtain 1D diffractograms [33,34]. LaB_6 was used for peak position and peak broadening calibration.

The 1D diffractograms obtained after pre-processing of the XRD patterns – in both *in-situ* and *ex-situ* experiments – were subjected to a refinement procedure to extract peak positions and peak areas. The refinement sequence consisted of subtracting the background signal from the diffractograms, identifying the peaks, and fitting them using a Pseudo-Voigt function. The peak areas were used to determine the volume fraction of austenite, following the quantification methods described elsewhere [35,36].

Furthermore, the austenite carbon content (c_γ) was calculated for the ex-situ diffraction data using the empirical Dyson and Holmes [37] equation, which correlates the austenite composition with its lattice parameter. It must be noted that the Dyson and Holmes equation does not account for the influence of silicon, as this element has a low impact on the austenite lattice parameter [38]. For c_γ calculation, partitioning of the substitutional elements between martensite and austenite was considered negligible during tempering (paraequilibrium). Therefore, the Mn and Cr contents used to determine c_γ were the same as those calculated for austenite in equilibrium at 865 °C, as shown in Table 1.

For microstructural characterization, samples were subjected to standard metallographic surface polishing down to 0.05 μm colloidal silica and then etched with 2% Nital solution (98 vol.% alcohol + 2 vol. % HNO_3). The microstructural features were observed and imaged with a field-emission gun scanning electron microscope (FEG-SEM) FEI Inspect F50, operated at an acceleration voltage of 20 keV. Microhardness testing was conducted using a load of 2.943 N and an indentation time of 15 s. Average hardness and standard deviation values were obtained from 20 indentations for each tempering condition.

Atom probe tomography (APT) was used to determine the carbon content and distribution of selected samples after 30 min tempering at 300 and 400 °C. Needle-shaped APT specimens were prepared using an FEI Helios Nanolab 600i dual-beam FIB/SEM instrument. The specimens were extracted from the surface of the bulk material using the FIB lift-out procedure suggested by Thompson et al. [39], mounted on the top of commercial Si micro-tips, and sharpened by annular ion milling. APT was performed on a LEAP 5000 XS (straight flight path) at a base temperature of 60 K in laser-pulsed mode at 40 pJ pulse energy. The wavelength, pulse rate and detection rate of the laser were 355 nm, 500 kHz and 1.5%, respectively. Reconstruction was carried out using commercial software (Cameca IVAS®) following the protocol introduced by Geiser et al. [40].

3. Results

3.1. Characterization of the as-quenched microstructure

Fig. 2a shows the as-quenched microstructure. The dark gray portion of the microstructure corresponds to the carbon supersaturated fresh martensite and retained austenite ($\alpha'_f + \gamma_R$) matrix, whereas the bright rounded particles correspond to the pro-eutectoid (*primary*) cementite. The latter is homogeneously dispersed and exhibits an average particle diameter of 175 ± 67 nm, as observed in more detail in the insert of Fig. 2a. The M_S temperature measured by dilatometry was detected at around 133 °C, followed by an incomplete martensitic transformation down to room temperature.

Fig. 2b details the high-resolution SXRD pattern of the as-quenched microstructure. Several peak convolutions exist, as indicated by black arrows. A triple convolution of $\{111\}\gamma_R$, $\{101\}\alpha'_f$, and $\{110\}\alpha'_f$ appears around 2.05 Å. Semi-convoluted $\{002\}\alpha'_f$ with $\{200\}\alpha'_f$, and $\{211\}\alpha'_f$ with $\{112\}\alpha'_f$ peaks were observed around 1.44 and 1.17 Å, respectively. Individual γ_R peaks also appear at 1.8, 1.26, and 1.08 Å. Shallow intensity peaks of cementite appear near the background level, as depicted by the green dashed detail in Fig. 2b. Cementite peaks are indicated by blue arrows and can be related to the as-quenched spheroidized cementite. There is no clear evidence of transition carbides via SXRD.

3.2. Microstructural evolution upon continuous heating

Fig. 3 presents the volumetric dilation measured during continuous heating from room temperature up to 500 °C at a constant heating rate of 10 °C.s^{-1}. Representative SXRD spectra, between 2.2 and 1.9 Å, collected during the heating process, are also shown in Fig. 3. The decomposition of the $\{111\}\gamma_R$, $\{101\}\alpha'$ and $\{110\}\alpha'$ triple convolution can be observed. The loss of tetragonality causes a displacement of the $\{101\}\alpha'$ peak to lower interplanar spacing, while the opposite occurs for $\{111\}\gamma_R$. At 250 °C, the $\{111\}\gamma_R$ and $\{101\}\alpha'$ are better resolved, and complete peak deconvolution is achieved at 450 °C. Besides, $\{101\}\alpha'$ achieves the $\{110\}\alpha'$ peak position during heating and becomes one unique martensite peak. The presence of $\{111\}\gamma_R$ peak is observed even before reaching 500 °C. Additionally, the derivative of the dilation curve shows that another contraction starts at ≈ 380 °C.

The kinetics of α' and γ_R decomposition and the evolution of the lattice parameters of γ_R and α' between 200 and 700 °C are presented in Fig. 4. Calculations below 200 °C are not presented due to the previously described triple convolution observed in Fig. 2a and also due to the absence of peaks with interplanar spacing lower than that of the $\{200\}\alpha'$ peak. Notice that the thermal resolution during continuous heating is 5.1 °C, associated to the detector exposure time of ≈ 6 s. The volume fraction of γ_R (solid black circles) remains constant up to 400 °C. Then, γ_R decomposition starts approximately at 400 °C, achieving its

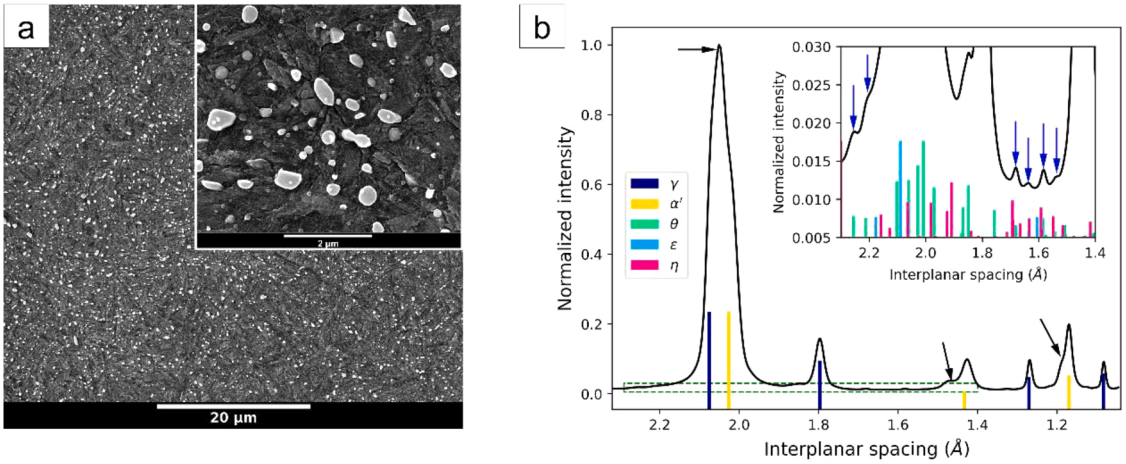

Fig. 2. (a) Scanning electron micrograph after cooling from 865 °C to room temperature. (b) High-resolution diffraction pattern of the initial condition. Black arrows indicate the splitting of martensite peaks, which occurs due to the high martensite tetragonality. Blue arrows indicate the peaks that cannot be indexed as either martensite or austenite, therefore being associated to carbides.

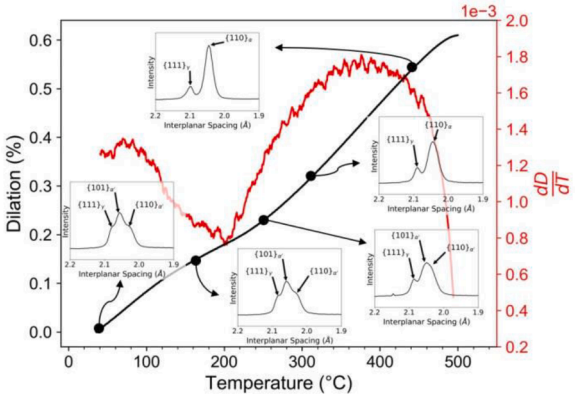

Fig. 3. Temperature vs. relative dilation during heating to the partitioning step showing the separation of the {111}γ, {101}α', and {110}α' peaks with increasing temperature. The red curve shows the derivative of the dilation curve.

completion at 600 °C.

The lattice parameter of γ_R shows a linear thermal expansion between 200 and 300 °C, whereas the lattice parameter of α' remains constant. Above 300 °C, both γ_R and α' show expansion behaviors. The lattice expansion rate of α' and, especially, of γ_R decreases between 400 and 500 °C. Between 500 and 600 °C, the lattice parameter of γ_R remains mostly unchanged despite the additional heating until its complete decomposition. Simultaneously, the lattice parameter of α' increases linearly with temperature up to 700 °C. Three stages of γ_R lattice parameter evolution can be identified, being 200–300 °C, 300–425 °C, and above 425 °C. To further study the time-resolved evolution of the as-quenched microstructure, seven temperatures (200, 250, 300, 350, 400, 450, and 500 °C) were selected for isothermal tempering experiments. These temperatures are represented as vertical dashed lines in Fig. 4.

3.3. Microstructural evolution during isothermal tempering

Fig. 5 details the dilation response curves for all isothermal tempering cycles between 200 and 500 °C. In Fig. 5a, both the heating and isothermal stages are shown, while in Fig. 5b only the isothermal stage is presented. In Fig. 5b, the dilation curves were shifted along the

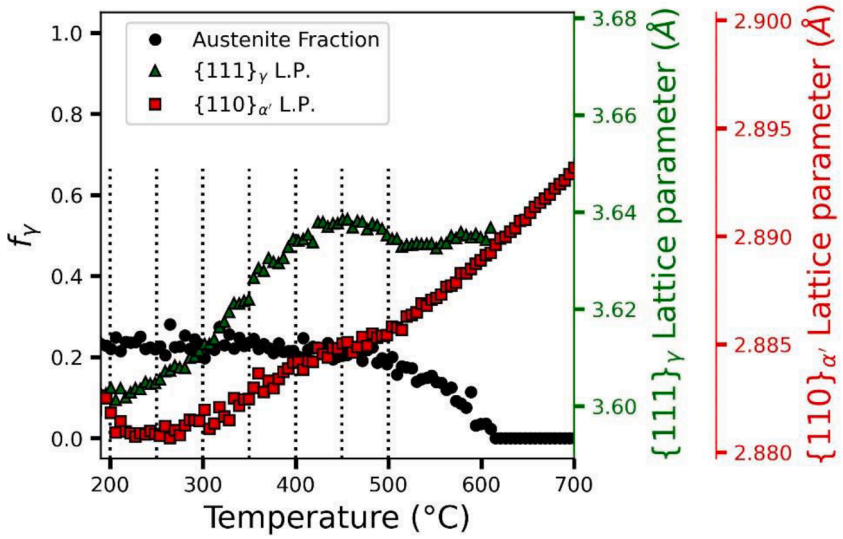

Fig. 4. Continuous heating from quenched condition (Fig. 2) showing: austenite volume fraction, austenite lattice parameter, and martensite lattice parameter temperature dependence. Heating rate: 0.833 °C.s^{-1}.

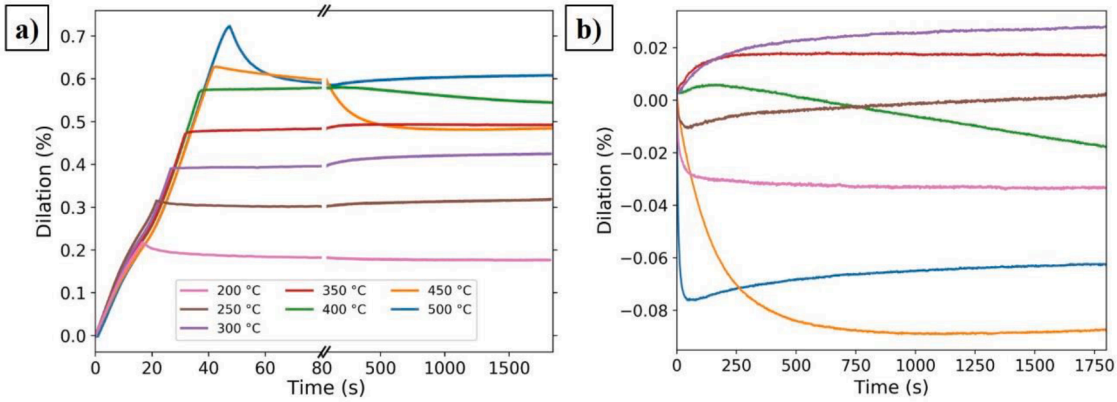

Fig. 5. Relative dilation for: a) the heating and isothermal stages of tempering; b) only the isothermal stage of tempering. The isothermal stages corresponded to temperatures of 200, 250, 300, 350, 400, 450, and 500 °C. The tempering time was set to 1800 s. The point zero relative dilation in b) was set as the time when the isothermal temperature was achieved.

y-axis, so they all coincide at the origin at the instant in which the respective isothermal temperatures are reached. During heating, a non-linear expansion occurs between room temperature and 250 °C, same behavior previously shown in Fig. 3. Above 250 °C, the volumetric expansion is linear upon continuous heating.

During the isothermal tempering stages, shown in Fig. 5b, the dilation curve for the 200 °C condition shows an initial fast contraction up to ≈ 500 s. For longer times, no change in the dilation response is seen. At 250 °C, a smaller contraction within the first 35 s is noticed, followed by a slight and steady expansion in the remaining holding time. During tempering at 300 °C, continuous volumetric expansion occurs, while at 350 °C, the volumetric expansion stagnates after ≈ 250 s. For temperatures above 400 °C, volumetric contraction becomes again noticeable. At 400 °C, the expansion stage occurrs in the first 100 s, followed by continuous contraction. At 450 °C, a significantly larger contraction occurs within the first 1000s, followed by stagnation for the remaining holding time. The fastest volumetric contraction occurs at 500 °C during the first 55 s of isothermal tempering, followed by a secondary expansion.

The time-resolved volume fraction of γ_R, as well as the lattice parameter evolution of γ_R during the isothermal soaking stages are shown in Fig. 6a and b, respectively. The lattice parameter is presented as a relative change with respect to the initial value observed at the very beginning of the isothermal soaking stage.

For tempering temperatures between 200 and 400 °C, the volume fraction of γ_R showed little to no variation. A noticeable decrease in the γ_R fraction up to ≈ 0.10 – associated with γ_R decomposition – occurred at the tempering temperature of 450 °C. A faster austenite decomposition was observed during tempering at 500 °C, achieving a volume fraction of ≈ 0.05 after 1000 s. Due to the faster decrease in the intensity of the {200}γ peak, the diffraction patterns presented only two martensite and one austenite measurable peaks. For this reason, Fig. 6a does not present data for tempering at 500 °C for longer times.

The relative evolution of the austenite lattice parameter (Δa_γ) clearly shows a dependence on the tempering temperature. At 200 °C, no significant variation is observed. However, at 250 and 300 °C, the lattice parameter monotonically increases with time, with the largest change happening at 300 °C. At 350 and 400 °C is noted a slight decrease in a_γ. At 450 and 500 °C, the lattice parameter decreases fast within the first 100 s of isothermal tempering. After ≈ 100 s, the {111}γ peak becomes too small to be measured accurately due to the fast austenite decomposition and the correct peak position determination is compromised.

3.4. Microstructural analysis after tempering

3.4.1. Carbon partitioning analysis by atom probe tomography

The elemental distribution analysis through α'/γ_R interfaces after 30 min tempering at 300 and 400 °C is summarized in Figs. 7 and 8, respectively. Fig. 7a shows the distribution of C ions, where the C-poor and C-rich regions correspond to α' and γ_R, respectively. Fig. 7b presents the 1D compositional analysis for C, Si, Mn, and Cr. This profile is relative to a cylindric region of interest (ROI), parallel to the long direction of the tip, crossing the α'/γ_R interface. Strong C partitioning at the γ_R is clearly noticed, with a maximum content of ≈ 8 at.% at the α'/γ_R interface. This value continuously decreases toward the austenite core, achieving a minimum of ≈ 5 at.%. Negligible partitioning of Cr and

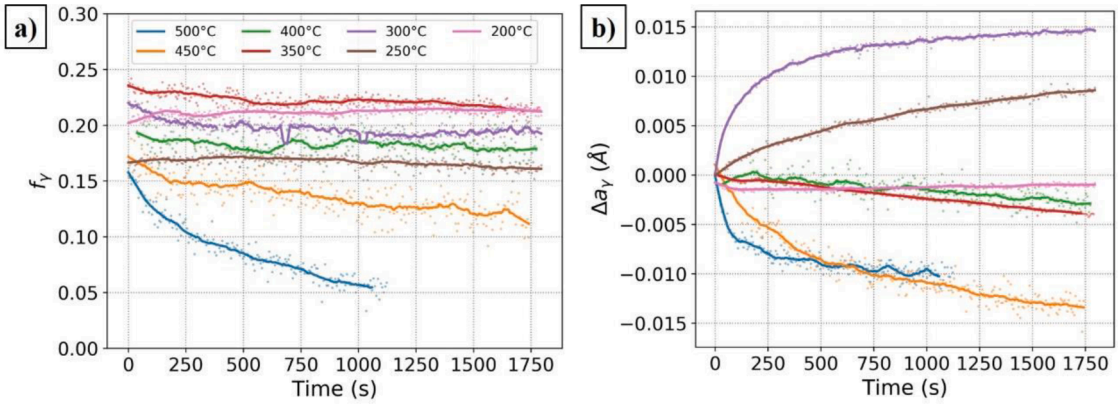

Fig. 6. In-situ quantitative SXRD results during the isothermal tempering stage showing: (a) austenite volume fraction; and (b) austenite lattice parameter variation. The point zero of figure (b) was assumed as the time when the material achieved the tempering temperature.

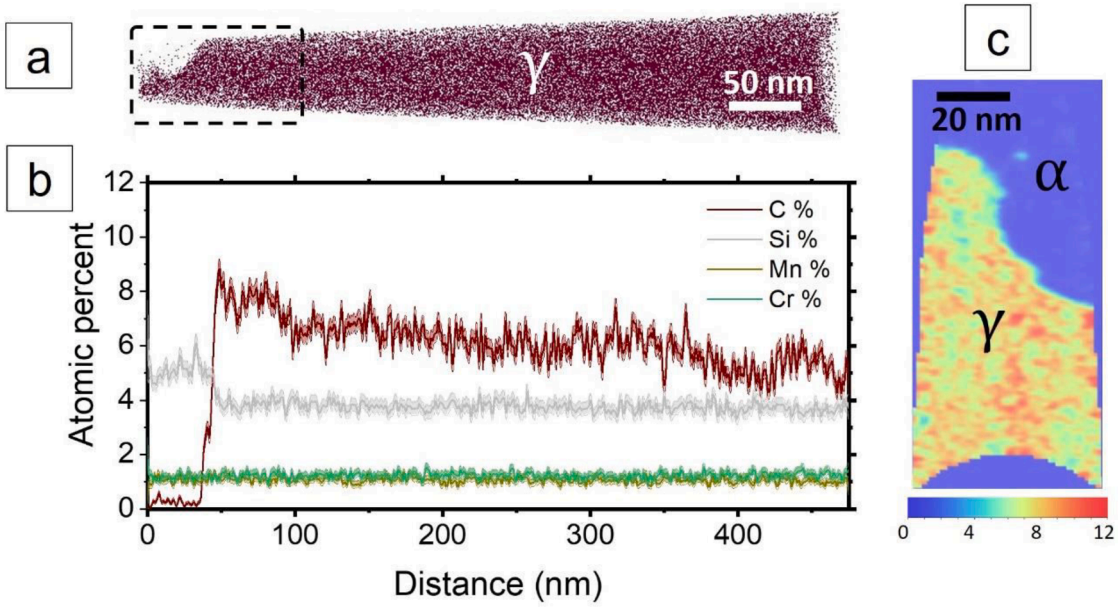

Fig. 7. Atom probe analysis obtained after tempering at 300 °C for 30 min showing: (a) Qualitative carbon map in the α'/γ interface region; (b) Proxigram results for C, Si, Mn, and Cr along cylinder region A shown in (a); (c) Heat map for carbon content obtained from the selected area showed in (a). The scale bar shown in (c) is related to at.% in carbon.

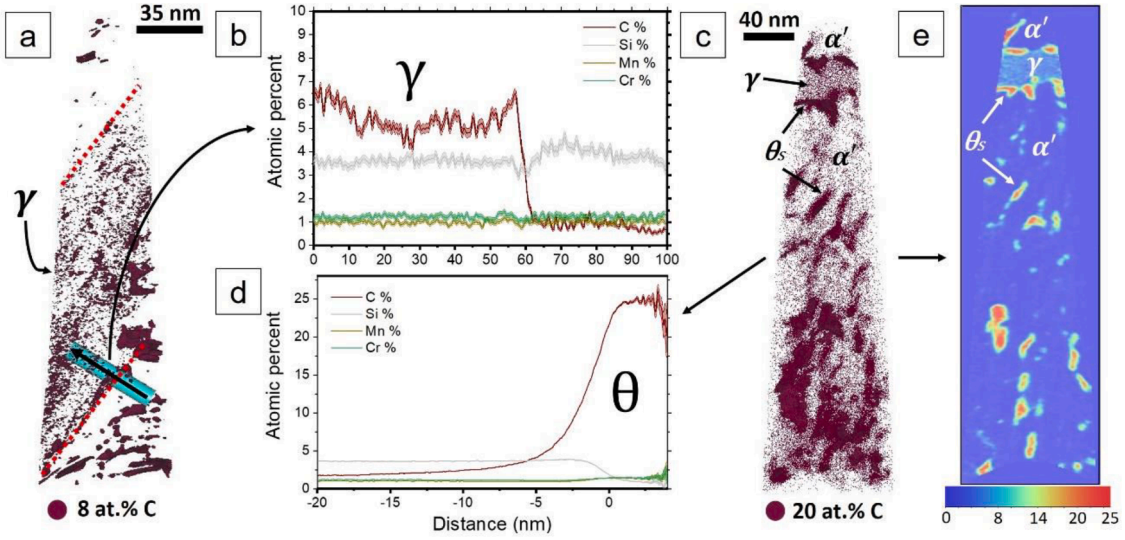

Fig. 8. Atom probe analysis obtained after tempering at 400 °C for 30 min showing: (a) qualitative carbon distribution of tip 1 analyzed with an isosurface carbon concentration of 8 at.%; (b) proxigram results for C, Si, Mn, and Cr along the ROI showed in (a); (c) qualitative carbon distribution of tip 2 analyzed with an isosurface carbon concentration of 20 at.% C; (d) proxigram results for C, Si, Mn, and Cr of tip 2 showed in (c); (e) heat map for carbon content obtained from tip 2 highlighting the presence of carbides. The scale bar in (e) is related to at.% in carbon.

Mn between phases and partitioning of Si into the α' are observed. Besides the inhomogeneous distribution of carbon, no apparent presence of cementite is evidenced by the carbon heat map depicted in Fig. 7c.

The APT results after tempering at 400 °C for 30 min are summarized in Fig. 8. The distribution of C ions, as well as the presence of several 8 at.% C isosurfaces highlighting C-rich regions within α' and γ_R are shown in Fig. 8a. In this case, a γ_R region between two martensite plates can be observed in the middle of the APT tip. Fig. 8b presents the 1D compositional analysis across the cylindric ROI shown in Fig. 8a. An inhomogeneous distribution of C within the γ_R can be noticed. Concentrations as high as ≈ 7 at.% C are found preferentially at the α'/γ_R interface, whereas at γ_R core, the concentration is only ≈ 5 at.%.

Similar to the microstructure after tempering at 300 °C, partitioning of Cr and Mn between α' and γ_R can be disregarded, while Si is preferentially observed within the α'. However, at 400 °C, nano-sized carbide precipitation occurs, as depicted in Fig. 8c by the 20 at.% C isosurfaces. A proxigram compositional analysis averaging an enveloped carbide particle is shown in Fig. 8d. The presence of 25 at.% C indicates that these carbide particles match the stoichiometry of θ cementite (Fe_3C). In addition, depletion of Si into θ is noticed. In the carbon heat map shown in Fig. 8e, precipitation of cementite is observed inside the martensite phase and also at the α'/γ_R interface.

3.4.2. Morphology and microstructural features of the observed microconstituents

Fig. 9a-d present SEM-SE images of the microstructure after

tempering cycles at 200, 300, 400, and 500 °C, respectively. All tempering conditions show primary spheroidized cementite, inherited from the intercritical austenitization (Fig. 2b). This type of carbide is here represented with the symbol θ_P to differentiate it from the secondary carbides originated from the decomposition of α'_f and γ_R (θ_S). After tempering at 200 and 300 °C, the microstructure consists of θ_P, γ_R, and α'. Martensite is distinctively etched, but no clear signs of secondary carbides precipitated in martensite are observed. After tempering at 400 and 500 °C, as shown in Figs. 9c and 9d, secondary carbides θ_S are observed in the α' matrix, as well as at the α'/γ_R interface boundaries. This is clearer noticed at 500 °C. At 500 °C, almost all the blocky γ_R decomposes, as well as the {200}γ peak appears with very low intensity (Fig. 9e). The blocky austenite decomposition during tempering at 500 °C leads to the precipitation of fine spheroidized and lamellar θ_S.

Ex-situ high-resolution XRD measurements of the as-quenched and tempered states are shown in Fig. 9e. The diffractograms detail the low-intensity carbide peaks near the background signal. A comparative microstructural condition consisting of a subcritical annealing cycle at 700 °C during 8 h (tempering at high temperature - THT) was performed to maximize the intensity of the θ peaks and completely eliminate the presence of retained austenite. This is helpful to assist in the interpretation of the degree of completion of secondary precipitation of θ_S at the selected tempering conditions. Black arrows in Fig. 9e indicate the positions of the equilibrium θ_S peaks, which are consistent with the peak positions of the θ_S peaks appearing during tempering. Cyan and purple lines represent the theoretical positions of η and ε transition carbides. However, there is no clear evidence of the presence of these two non-equilibrium precipitates. The increased intensity of θ peaks can be associated mainly to both martensite tempering and γ_R dissolution, as confirmed by the APT observations presented in Fig. 8e.

Fig. 9f shows a summary of the volume fraction of γ_R, its carbon content and the overall microhardness after tempering. Hardness was added to Fig. 9f for a more comprehensive understanding of the microstructural evolution. The γ_R fraction was calculated excluding the presence of {111}γ, {101}α', and {110}α' peaks due to complex peak convolution (refer to Fig. 2c). The as-quenched condition presents peak convolutions at each martensite peak position. This might result in an underestimation of the γ_R fraction, and for that reason, it was plotted as an open star symbol in Fig. 9f. The austenite carbon content was calculated based on the austenite peak positions [37] (also excluding the {111}γ peak). The blue dashed horizontal line in Fig. 9f represents the austenite carbon composition at 865 °C calculated by the CALPHAD method.

The as-quenched microstructure presents a maximum hardness of 837 ± 12 HV and a volume fraction of γ_R of 25%. The experimentally determined carbon content is lower than the calculated value. A slight hardness reduction to 794 ± 13 HV occurs after tempering at 200 °C due to the beginning of martensite tempering. Tempering between 250 and

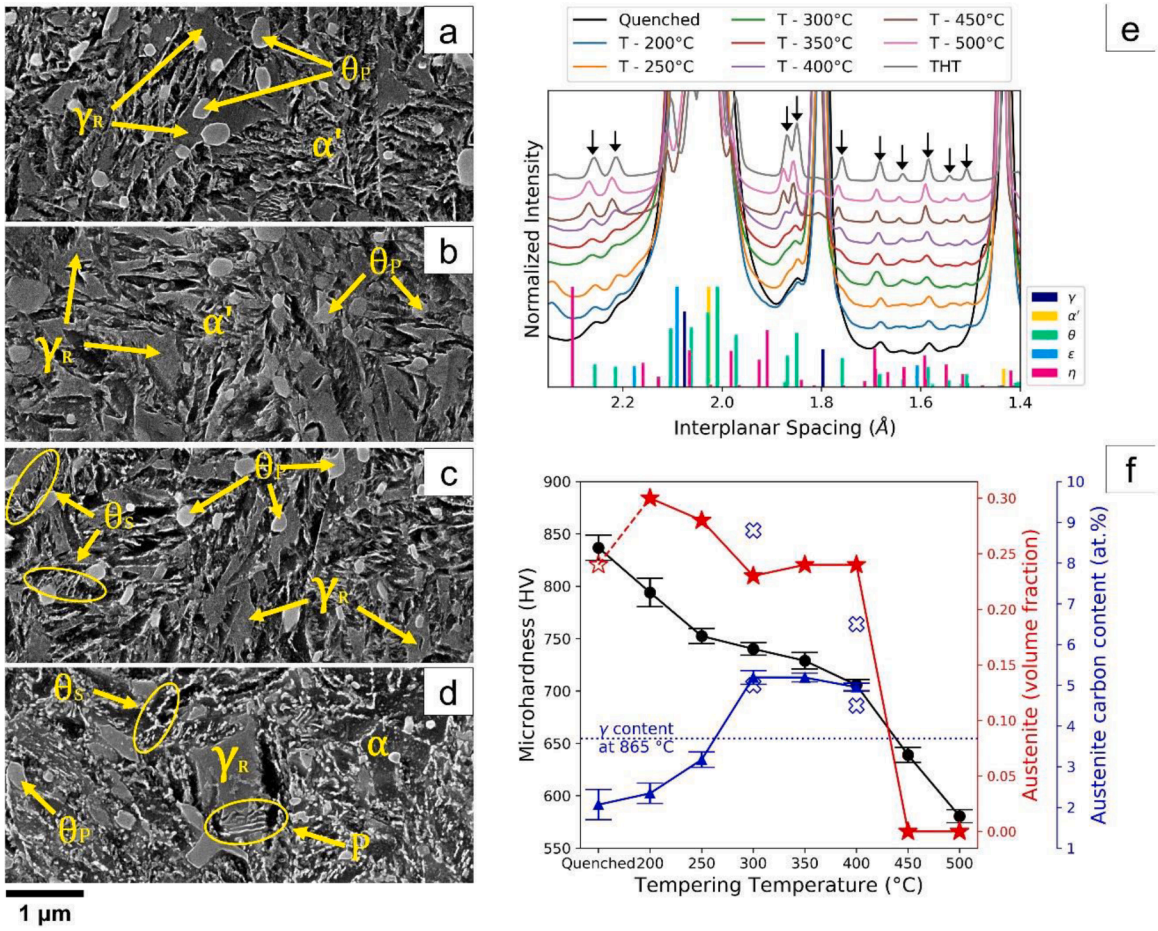

Fig. 9. Ex-situ results after tempering at different temperatures for 1800s. Scanning electron microscopy after intercritical annealing at 865 °C, followed by quenching to room temperature and tempering at: (a) 200 °C, (b) 300 °C, (c) 400 °C, and (d) 500 °C. (e) Low-intensity peaks obtained by high-resolution synchrotron diffraction in transmission mode diffraction geometry. (f) Microhardness, austenite volume fraction, and austenite carbon content temperature dependence. The vertical-colored lines in figure (e) are related to the different peak positions obtained from crystallographic files patterns. The ratio intensity of the peaks of each phase was preserved for better comparison. The open star in figure (f) is related to inaccuracy of the measurement due to presence of tetragonal martensite and convolution of the peaks. The open x symbols in figure (f) at 300 and 400 °C are related to carbon content at the austenite interface (higher value) and core (lower value) obtained by APT measurements, as will be shown in the following results.

350 °C results in additional softening to 729 ± 8 HV. Slight reduction in the volume fraction of γ_R is accompanied by austenite carbon enrichment from 2.34 ± 0.25 at.% at 200 °C to 5.19 ± 0.11 at.% at 350 °C. Tempering above 400 °C results in a noticeable decrease in hardness, achieving values as low as 580 ± 6 HV after tempering at 500 °C. This behavior occurs by the complete dissolution of γ_R and forming a soft tempered martensite matrix with a large fraction of θ_P and θ_S. The austenite carbon content at 450 and 500 °C is not presented due to the very low intensities of FCC peaks after tempering at these temperatures.

The γ_R carbon contents measured by APT at the γ_R/α' interfaces and at the core of the γ_R regions are shown in Fig. 9f as blue open crosses. The carbon at the γ_R/α' interface is significantly higher than that determined by SXRD. However, the APT measured carbon contents at the γ_R core are in good agreement with the SXRD values. This gradient-like behavior indicates the transient nature of the carbon partitioning for the heat treatment conditions.

4. Discussion

4.1. Martensite tetragonality and its decrease during carbon redistribution

Fig. 3 shows that besides the self-tempering, pairs of BCT martensite peaks are clearly visible at room temperature ({110}α' and {101}α' peaks). These diffraction patterns are well correlated to the dilation curve during heating, showing that the small contraction during heating is due to the decreasing of martensite tetragonality caused by carbon redistribution. Cheng et al. [41] inferred by dilation and calorimetric results that the small contraction observed during low temperatures of tempering is related to the redistribution of carbon atoms to dislocations and twin boundaries of martensite. This carbon redistribution can be drawn from the present results. Carbon leaves octahedral martensite sites and fills dislocation sites. It decreases the martensite tetragonality.

The c/a ratio calculated from the {002}α' and {200}α' peaks is 1.0313. According to empirical Nishiyama equation [42], which establishes a relationship between the c/a ratio and austenite chemical composition, and using austenite chemical composition in equilibrium at 865 °C (Table 1), a c/a ratio of 1.0375 is expected for the as-quenched martensite. Conversely, the martensite carbon content calculated from the c/a ratio is 0.696 wt.%, which is 0.138 wt.% lower than the parent austenite carbon content (0.834 wt.%). This difference suggests that carbon redistribution took place during the quenching stage. Speich and Leslie [43] showed that dislocations in martensite are saturated at approximately 0.2 wt.% of carbon. Therefore, a remaining 0.062 wt.% of carbon could still redistribute to martensite dislocations, about 1/3 of all carbon that can saturate martensite dislocations. During further heating to tempering temperature (refer to Fig. 3), a slight deviation from linear expansion is observed in the dilation curve at ≈ 170 °C. This temperature is the same where martensite tetragonality decreases. Cheng et al. [41] already showed that the slight contraction observed before the first stage of tempering of martensite is related to carbon redistribution. In our work, as 0.062 wt.% of carbon still can diffuse to dislocations, it is reasonable to assume that the slight deviation in the dilation curve during the heating is associated with carbon segregation in martensite.

4.2. Microstructural decomposition during the isothermal stage of tempering

The isothermal stage of tempering at 200 °C and 250 °C (see Fig. 5) starts with a contraction which seems to be the continuity of tetragonality decrease and carbon redistribution of martensite. Cheng et al. [41] calculated the volume change associated with the different tempering stages and found that the carbon redistribution and segregation cause the smallest volume change in tempering, consistent with the present findings. The results still show that the contraction at the beginning of isothermal holding at 250 °C is smaller than at 200 °C. This is reasonable, considering that more carbon diffusion occurred in the heating between 200 and 250 °C.

For temperatures equal to or above 300 °C, the isothermal stage begins after the contraction during heating has finished. This indicates that the first stage of tempering is completed before 300 °C is achieved. The presence of only expansion during tempering at 300 and 350 °C suggests that austenite is decomposing. Santofimia et al. [44] showed that γ/α' interface migration due to carbon partitioning can lead to an expansion in the dilation curve. However, even if most of the expansion was related to the interface migration, it would be expected that the austenite volume fraction would increase during tempering [16]. The *in-situ* SXRD results for tempering at 300 °C show that, although a_γ increases, the f_γ decreases slightly during the first seconds of the isothermal stage (refer to Fig. 5a and b). Thus, it is likely that some austenite decomposition to bainite occurs.

For tempering at 350 and 400 °C, a slight decrease in the austenite volume fraction in the isothermal stage is also observed (Fig. 6a). However, opposite to what happens at 300 °C, the a_γ decreases (Fig. 6b). This is surprising, as either interface migration or bainite formation would lead to austenite carbon enrichment, which should be reflected as an increase in a_γ. This behavior suggests that austenite is at first enriched in carbon due to either carbon diffusion from martensite and bainite (due to the partially austenite decomposition into ferritic bainite) and subsequently the austenite is decomposed into carbide.

At 400 °C, after a short expansion, the material contracts. Similar results were found by Wang and Huang [45] for tempering temperatures between 400 and 500 °C. Analyzing in-situ the tempering of a conventional SAE 52100 steel at 340 °C by synchrotron radiation of high energy, Foster et al. [46] observed only a contraction during the isothermal stage, at the same time that austenite was almost entirely decomposed in 30 s after achieving the tempering temperature. The opposite behavior found in the present work shows that the alloying with silicon was sufficient to open a window process to carbon partitioning as austenite almost did not decompose after tempering at 300 and 350 °C.

During tempering at 450 °C, a significant contraction is observed. Following the events observed up to this temperature, it is reasonable to infer that carbide formation is occurring during contraction at 450 °C. Jung et al. [47] already mentioned that the cementite precipitation in the third stage of tempering leads to a high contraction in the dilatometric curve. They also stated that this cementite is mainly nucleated at carbon clusters inside twins in martensite, as well as from transition carbides previously formed. It decreases the strain lattice due to lower carbon saturation and consequently, lowers martensite volume. A similar contraction is observed at 500 °C, followed by a small expansion. As a_γ and f_γ rapidly decrease, the sequence of phenomena is related to cementite precipitation inside martensite, destabilization of austenite by loss of carbon, and transformation of unstable remaining austenite into an eutectoid product (pearlite-like) (see Fig. 9d). The decomposition of austenite to pearlite during tempering at high temperatures was previously reported by Wang and Huang [45]. Recently, Ayenampudi et al. [27] showed that pearlite does indeed form during partitioning at temperatures above 500 °C. The authors carried out partitioning step for up to 3600 s and discussed the amount of pearlite formed using a combination of techniques such as XRD, dilatometry, and SEM.

4.3. Effect of tempering temperature on the final microstructure

Henceforward focus is given to the final microstructure. The microstructures after tempering at 200 and 300 °C (refer to Fig. 9a and b) do not show any noticeable difference. The microstructural differences associated at these tempering temperatures would only be observed at a finer scale. The SXRD austenite carbon content measured for the as-quenched condition shows that the results are not just related to the influence of carbon partitioning. The carbon content calculated from the a_γ (Fig. 9f) shows values lower than those calculated at the intercritical temperature. The retained austenite and martensite were expected to present the same chemical composition, i.e., the austenite composition

calculated at 865 °C. Two possible reasons could lead to this observation: (i) austenite loses carbon due to some instability or decomposition during quenching; or (ii) some phenomenon that is not regarded in the calculation of the carbon composition from the austenite peak position is present, leading to an imprecise carbon content value.

Cheng et al. [48] found that as higher fraction of martensite volume is formed, the lower the austenite carbon content (c_γ) measured by XRD. The authors explained that this observation resulted from hydrostatic compression of retained austenite. As more martensite forms, more retained austenite will be under compression. Epp [49] used SXRD to show the influence of compression of austenite on the calculated c_γ. He found that a_γ decreases linearly until the M_S temperature; once the M_S is reached, the lattice parameter decreases at a higher rate, meaning that lower c_γ are calculated. Cheng et al. [48] attributed the decreasing in the calculated c_γ to the triaxial stresses being applied in austenite. Therefore, the c_γ found by SXRD for the quenched condition in our work is not the actual of retained austenite, but a value that is influenced by the high hydrostatic compression that austenite experiences. Then, it is reasonable to assume that the austenite presents the same carbon content as at the equilibrium at 865 °C.

Temperatures equal to or above 450 °C are shown to be high enough to destabilize austenite and promote its decomposition. The corresponding microstructure shows that secondary carbides are more developed and distributed in the matrix after tempering at 450 °C. At 500 °C, even cooperative eutectoid product was found as it showed to be formed from a block of retained austenite. For those temperatures, austenite carbon enrichment control is very difficult, if still possible, and no window to this phenomenon was detected.

Due to the austenite carbon enrichment, increasing its stability, combined with a high hardness (> 700 HV), the tempering temperature range between 300 and 400 °C seems to be the best to improve the austenite stability. As can be seen in Fig. 7, the tempering phenomenon involved during tempering at 300 °C appears to be mainly carbon partitioning from α' to γ_R, where α' can be either martensite or some supersaturated ferritic bainite formed during the tempering. As shown by the APT results, the inhomogeneous carbon distribution in austenite reveals that longer times are required to achieve a homogeneous carbon distribution inside austenite. The increase in the silicon content in martensite close to the α'/γ_R interface is similar to that found by other authors [50,51]. However, no enrichment of manganese or chromium was found along the α'/γ_R interface, indicating that this combination of time/temperature was not enough to allow their diffusion. Even though precipitation of tempering carbides in martensite was not evident by APT measurements in this condition, it could have happened, causing a Si partitioning between martensite and the carbides. The Si partitions through the interface would imply a movement of the interface, which seems to not be occurring. In Fig. 8, which shows the APT analysis for tempering at 400 °C, secondary carbides that precipitated in martensite are clearly visible. These carbides are expected to have a lower Si solubility with respect to martensite, meaning that their formation would cause an increase of Si in martensite. So, in this case, it is reasonable that the increased Si in martensite is not caused by a Si partition between martensite and austenite, but rather between martensite and the (secondary) carbides. The lower c_γ after tempering at 400 °C (4–7 at.%) (see Fig. 8), with a similar silicon pile-up being observed at the α'/γ_R interface, show that carbon partitioning appears to have achieved its limit and austenite decomposition to cementite takes place. Thus, silicon is not effective in delaying cementite formation anymore.

4.4. Carbon partitioning – thermodynamic limits

Several models for the carbon partitioning between martensite and austenite have been proposed after that of Speer et al. [12]. The CCEθ model proposed by Toji et al. [19] is particularly interesting for high carbon steels, as it accounts for the Gibbs energy change that occurs due to carbide precipitation. Unlike Speer, the CCEθ model considers martensite and carbide in a metastable equilibrium, while this mixture establishes an equilibrium with austenite with respect to carbon, only. As a result, the final austenite carbon composition depends on the carbide Gibbs energy. Thus, the carbide type becomes a critical factor in understanding the carbon partitioning mechanism. As in Toji's work, for the present analysis, two types of cementite are assumed: paracementite, i.e., cementite in paraequilibrium with martensite, and orthocementite, cementite in full equilibrium with martensite.

The comparison between the experimental values of c_γ (measured by SXRD) with the CCEθ model is shown in Fig. 10. The scattered dots with error bars represent the experimentally measured c_γ. The black and red solid lines represent the carbon content of austenite in the condition of ortho and para equilibrium between martensite and carbides, respectively. Furthermore, austenite carbon content measured by APT at the austenite interface and core are shown as open and filled black star symbols, respectively. In the CCEθ model, the α' + θ mixture establishes with γ an equilibrium with respect to carbon. The chemical potentials of carbon in martensite, cementite, and austenite must be the same. As a consequence, carbides with higher free energy (translated as a higher carbon chemical potential) will lead to higher austenite carbon content values. As a matter of fact, it can be seen that austenite can be either depleted or enriched in carbon depending on the carbide's Gibbs energy. While orthocementite leads to an austenite with a lower carbon content than the original composition, paracementite leads to carbon enrichment.

As barely noticeable austenite peaks were observed in the SXRD measurements after tempering at 450 and 500 °C, it was not possible to measure c_γ at these conditions. At low tempering temperatures (200 and 250 °C), the c_γ values are lower than the initial austenite composition. However, it is well known that transition carbides are expected to form at low temperatures, rather than orthocementite. The reason for such low c_γ values at 200 and 250 °C could be explained by the shifting of austenite diffraction peaks to lower interplanar spacings due to hydrostatic pressure, which is caused by martensite forming around austenite. The austenite carbon content increases at higher temperatures (300–400 °C), becoming higher than the initial composition, however still far from paracementite consideration. It is noted from Fig. 9f that c_γ decreases slightly from 300 to 400 °C. This decrease is explained by the increased likelihood of precipitation of cementite, a carbide with lower Gibbs energy than the transition carbides. Thus, this indicates that at higher temperatures, orthocementite in metastable equilibrium with

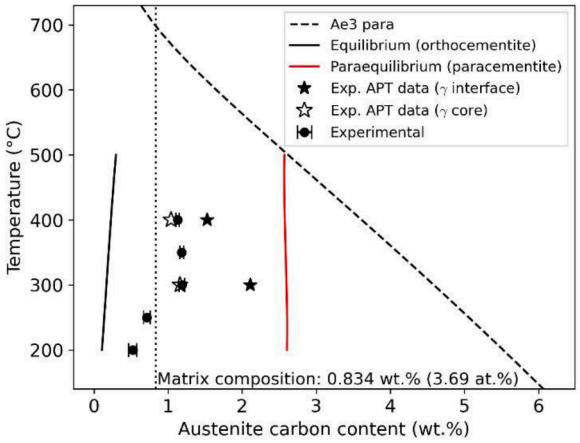

Fig. 10. Phase diagram with predicted austenite carbon compositions assuming the CCE model. Experimental data obtained from SXRD are shown as circles. The error bars are related to the standard deviation of carbon chemical content calculated using different austenite peaks. Filled and opened star symbols are the values obtained from APT measurements at the austenite interface and core, respectively. Black and red solid lines are expected austenite carbon content assuming equilibrium and paraequilibrium, respectively.

martensite will dictate the final austenite carbon composition.

The influence of primary cementite homogeneously dispersed in the matrix on the carbon partitioning between martensite and austenite seems to be of little effect. As these cementite particles were formed during intercritical annealing, they can be considered as orthocementite, which would lead the austenite to be depleted in carbon, according to Fig. 10. Although it is expected that carbon partitions to primary cementite, decreasing the carbon available to enrich austenite, it is noted a continuous austenite carbon enrichment up to 350 °C while no cementite appears to form inside martensite. Only at 400 °C, when secondary cementite precipitates inside martensite and at the austenite/martensite interfaces, austenite begins to lose carbon. Therefore, only the carbides formed during the tempering have significant influence on carbon partitioning path, i.e., austenite carbon enrichment or depletion.

5. Conclusions

In summary, the mechanisms behind retained austenite carbon stabilization and decomposition were clarified through a combination of *in-situ* synchrotron X-ray diffraction, contact dilatometry, scanning electron microscopy, microhardness, and atom probe tomography characterization. The times and temperatures required to achieve effective carbon partitioning into austenite, or microstructural decomposition into secondary cementite, were revealed.

The retained austenite phase undergoes little if any carbon partitioning below 200 °C even after 1800 s of isothermal soaking, while the fresh martensite tetragonality decreases in the range of 150–250 °C. Enough energy is given to allow carbon partitioning with tempering temperatures between 250 and 400 °C, leading to carbon partitioning from martensite to austenite. Carbon enrichment with minimum austenite decomposition is accelerated at 250 °C and maximized at 300 °C with most of the process occurring within the first 250 s of isothermal soaking. However, this trend is inverted at 350 °C, leading to austenite carbon depletion, which in turn leads to austenite destabilization and decomposition either isothermally or during quenching. At 400 °C, cementite precipitates inside martensite plates and at martensite/austenite interfaces. Above 450 °C, the kinetics of isothermal austenite decomposition accelerates, and the remaining undissolved fraction transforms into martensite upon quenching. A pearlite-like structure starts to appear after tempering at 500 °C.

The primary spheroidized cementite does not have significant influence on the kinetics of carbon partitioning into austenite. Despite the widespread presence of primary cementite, austenite continues to enrich in carbon between 250 and 350 °C without an apparent cementite coarsening. Contrasting, secondary cementite precipitation plays a major role as a competitive reaction, limiting the carbon availability for austenite enrichment above 350 °C.

The time-temperature-partitioning relationships revealed in this work through in situ microstructural observations can be beneficial for future heat treatment optimization of high silicon high carbon steels. These results offer a pathway to engineer microstructures targeting, for example, maximum austenite stability, minimum austenite presence, or even stress relief without volumetric phase evolution.

Declaration of Competing Interest

The authors declare that they have no known competing financial interests or personal relationships that could have appeared to influence the work reported in this paper.

Acknowledgments

This study was financed in part by the Coordenação de Aperfeiçoamento de Pessoal de Nível Superior - Brasil (CAPES) - Finance Code 001. JPO acknowledges funding by national funds from FCT - Fundação para a Ciência e a Tecnologia, I.P., in the scope of the projects LA/P/0037/2020, UIDP/50025/2020 and UIDB/50025/2020 of the Associate Laboratory Institute of Nanostructures, Nanomodelling and Nanofabrication – i3N. The authors acknowledge DESY (Hamburg, Germany), a member of the Helmholtz Association HGF, for providing the experimental facilities. Beamtime was allocated for proposal I-20210995 EC. This research used facilities of the Brazilian Synchrotron Light Laboratory (LNLS), part of the Brazilian Center for Research in Energy and Materials (CNPEM), a private non-profit organization under the supervision of the Brazilian Ministry for Science, Technology, and Innovations (MCTI). The X-ray Scattering and Thermo-Mechanical Simulation (XTMS) beamline staff is acknowledged for the assistance during the experiments proposals 20190225 and 20190049. The authors are grateful to U. Tezins and A. Sturm for their support to the FIB and APT facilities at MPIE. The research leading to this result has been supported by the project CALIPSOplus under the Grant Agreement 730872 from the EU Framework Programme for Research and Innovation HORIZON 2020. J.A. Avila is a Serra Hunter Fellow and a CNPq fellow. Escobar wants to thank FAPESP for the Post-Doctoral funding relative to the project 2018/21251-5.

References

[1] H.K.D.H. Bhadeshia, Steels for bearings, Prog. Mater. Sci. 57 (2012) 268–435, https://doi.org/10.1016/j.pmatsci.2011.06.002.
[2] J.A. Ciruna, H.J. Szieleit, The effect of hydrogen on the rolling contact fatigue life of AISI 52100 and 440C steel balls, Wear 24 (1973) 107–118, https://doi.org/10.1016/0043-1648(73)90207-X.
[3] S. Smith, S.N. Melkote, E. Lara-Curzio, T.R. Watkins, L. Allard, L. Riester, Effect of surface integrity of hard turned AISI 52100 steel on fatigue performance, Mater. Sci. Eng. A. 459 (2007) 337–346, https://doi.org/10.1016/j.msea.2007.01.011.
[4] J.A. Martin, S.F. Borgese, A.D. Eberhardt, Microstructural alterations of rolling-bearing steel undergoing cyclic stressing, J. Fluids Eng. Trans. ASME. 88 (1966) 555–565, https://doi.org/10.1115/1.3645902.
[5] Y.B. Guo, C.R. Liu, Mechanical properties of hardened AISI 52100 steel in hard machining processes, J. Manuf. Sci. Eng. Trans. ASME. 124 (2002) 1–9, https://doi.org/10.1115/1.1413775.
[6] J.G. Speer, E. De Moor, A.J. Clarke, Critical assessment 7: quenching and partitioning, Mater. Sci. Technol. (United Kingdom). 31 (2015) 3–9, https://doi.org/10.1179/1743284714Y.0000000628.
[7] N.V. Luzginova, L. Zhao, J. Sietsma, The cementite spheroidization process in high-carbon steels with different chromium contents, Metall. Mater. Trans. A Phys. Metall. Mater. Sci. 39 A (2008) 513–521, https://doi.org/10.1007/s11661-007-9403-3.
[8] C. Li, J.L. Wang, Effect of pre-quenching on martensite-bainitic microstructure and mechanical properties of GCr15 bearing steel, J. Mater. Sci. 28 (1993) 2112–2118, https://doi.org/10.1007/BF00367570.
[9] J. ping Lai, L. ping Zhang, W. Gong, X. Xu, C. an Xiao, J. ping Lai, L. ping Zhang, W. Gong, X. Xu, C. an Xiao, Two-body abrasion resistance of high carbon steel treated by quenching-partitioning-tempering process, Wear. 440–441 (2019) 203096. https://doi.org/10.1016/j.wear.2019.203096.
[10] T. Sourmail, F. Danoix, C. Garcia-Mateo, F.G. Caballero, R. Rementiera, L. Morales-Rivas, R.P. Sanz, R. Janisch, S. Sampath, I. Müller, E. Kerscher, M. Kuntz, Understanding Basic Mechanism to Optimize and Predict in Service Properties of Nanobainitic Steels (MECBAIN), European Comission, 2017, https://doi.org/10.2777/657047.
[11] N. Luzginova, L. Zhao, J. Sietsma, Evolution and thermal stability of retained austenite in SAE 52100 bainitic steel, Mater. Sci. Eng. A. 448 (2007) 104–110, https://doi.org/10.1016/j.msea.2006.10.014.
[12] J. Speer, D.K. Matlock, B.C. De Cooman, J.G. Schroth, Carbon partitioning into austenite after martensite transformation, Acta Mater.. 51 (2003) 2611–2622, https://doi.org/10.1016/S1359-6454(03)00059-4.
[13] J.G. Speer, D.V. Edmonds, F.C. Rizzo, D.K. Matlock, Partitioning of carbon from supersaturated plates of ferrite, with application to steel processing and fundamentals of the bainite transformation, Curr. Opin. Solid State Mater. Sci. 8 (2004) 219–237, https://doi.org/10.1016/j.cossms.2004.09.003.
[14] N. Saenarjhan, J.-.H. Kang, S.-.J. Kim, Effects of carbon and nitrogen on austenite stability and tensile deformation behavior of 15Cr-15Mn-4Ni based austenitic stainless steels, Mater. Sci. Eng. A. 742 (2019) 608–616, https://doi.org/10.1016/j.msea.2018.11.048.
[15] R. Xiong, H. Peng, S. Wang, H. Si, Y. Wen, Effect of stacking fault energy on work hardening behaviors in Fe-Mn-Si-C high manganese steels by varying silicon and carbon contents, Mater. Des. 85 (2015) 707–714, https://doi.org/10.1016/j.matdes.2015.07.072.
[16] M.J. Santofimia, L. Zhao, R. Petrov, C. Kwakernaak, W.G. Sloof, J. Sietsma, Microstructural development during the quenching and partitioning process in a newly designed low-carbon steel, Acta Mater.. 59 (2011) 6059–6068, https://doi.org/10.1016/j.actamat.2011.06.014.

[17] E.J. Seo, L. Cho, Y. Estrin, B.C. De Cooman, Microstructure-mechanical properties relationships for quenching and partitioning (Q\&P) processed steel, Acta Mater.. 113 (2016) 124–139, https://doi.org/10.1016/j.actamat.2016.04.048.
[18] X.H. Hu, X. Sun, L.G. Hector, Y. Ren, Individual phase constitutive properties of a TRIP-assisted QP980 steel from a combined synchrotron X-ray diffraction and crystal plasticity approach, Acta Mater.. 132 (2017) 230–244, https://doi.org/10.1016/j.actamat.2017.04.028.
[19] Y. Toji, G. Miyamoto, D. Raabe, Carbon partitioning during quenching and partitioning heat treatment accompanied by carbide precipitation, Acta Mater.. 86 (2015) 137–147, https://doi.org/10.1016/j.actamat.2014.11.049.
[20] Y. Toji, H. Matsuda, M. Herbig, P.P. Choi, D. Raabe, Atomic-scale analysis of carbon partitioning between martensite and austenite by atom probe tomography and correlative transmission electron microscopy, Acta Mater.. 65 (2014) 215–228, https://doi.org/10.1016/j.actamat.2013.10.064.
[21] M. Wendler, C. Ullrich, M. Hauser, L. Krüger, O. Volkova, A. Weiß, J. Mola, Quenching and partitioning (Q\&P) processing of fully austenitic stainless steels, Acta Mater.. 133 (2017) 346–355, https://doi.org/10.1016/j.actamat.2017.05.049.
[22] A.S. Nishikawa, G. Miyamoto, T. Furuhara, A.P. Tschiptschin, H. Goldenstein, Phase transformation mechanisms during Quenching and Partitioning of a ductile cast iron, Acta Mater. 179 (2019) 1–16, https://doi.org/10.1016/j.actamat.2019.08.001.
[23] M.J. Santofimia, J.G. Speer, A.J. Clarke, L. Zhao, J. Sietsma, Influence of interface mobility on the evolution of austenite-martensite grain assemblies during annealing, Acta Mater. 57 (2009) 4548–4557, https://doi.org/10.1016/j.actamat.2009.06.024.
[24] A.J. Clarke, J.G. Speer, M.K. Miller, R.E. Hackenberg, D.V. Edmonds, D.K. Matlock, F.C. Rizzo, K.D. Clarke, E. De Moor, Carbon partitioning to austenite from martensite or bainite during the quench and partition (Q\&P) process: a critical assessment, Acta Mater. 56 (2008) 16–22, https://doi.org/10.1016/j.actamat.2007.08.051.
[25] A.S. Nishikawa, M.J. Santofimia, J. Sietsma, H. Goldenstein, Influence of bainite reaction on the kinetics of carbon redistribution during the Quenching and Partitioning process, Acta Mater. 142 (2018) 142–151, https://doi.org/10.1016/j.actamat.2017.09.048.
[26] D.T. Pierce, D.R. Coughlin, D.L. Williamson, K.D. Clarke, A.J. Clarke, J.G. Speer, D. K. Matlock, E. De Moor, Mössbauer spectroscopy investigation of transition carbides in quenched and partitioned steel, in: PTM 2015 - Proc. Int. Conf. Solid-Solid Phase Transform. Inorg. Mater. 2015, Whistler, 2015, pp. 91–98.
[27] S. Ayenampudi, C. Celada-Casero, J. Sietsma, M.J. Santofimia, Microstructure evolution during high-temperature partitioning of a medium-Mn quenching and partitioning steel, Materialia 8 (2019), 100492, https://doi.org/10.1016/j.mtla.2019.100492.
[28] C. Celada-Casero, C. Kwakernaak, J. Sietsma, M.J. Santofimia, The influence of the austenite grain size on the microstructural development during quenching and partitioning processing of a low-carbon steel, Mater. Des. 178 (2019), 107847, https://doi.org/10.1016/j.matdes.2019.107847.
[29] R.A. Stewart, J.G. Speer, B.G. Thomas, E. De Moor, A.J. Clarke, Quenching and Partitioning of Plate Steels: partitioning Design Methodology, Metall. Mater. Trans. A Phys. Metall. Mater. Sci. 50 (2019) 4701–4713, https://doi.org/10.1007/s11661-019-05337-3.
[30] Z. Dai, Z. Yang, C. Zhang, H. Chen, Incomplete carbon partitioning during quenching and partitioning of Fe–C–Mn–Si steels: modeling and experimental validations, Acta Mater. 200 (2020) 597–607, https://doi.org/10.1016/j.actamat.2020.09.045.
[31] S. SHIKO, K. OKAMOTO, S. WATANABE, Effect of metallographical factors on rolling fatigue life of ball bearing steel, Iron Steel Inst. Japan-J 54 (1968) 1353–1366.
[32] E. Kozeschnik, H.K.D.H. Bhadeshia, Influence of silicon on cementite precipitation in steels, Mater. Sci. Technol. 24 (2008) 343–347, https://doi.org/10.1179/174328408X275973.
[33] A.P. Hammersley, FIT2D V12.012 Reference Manual V6.0 ESRF98HA01T, 2004. https://www.esrf.fr/computing/scientific/FIT2D/FIT2D_REF/fit2d_r.html.
[34] A.P. Hammersley, S.O. Svensson, M. Hanfland, A.N. Fitch, D. Hausermann, Two-dimensional detector software: from real detector to idealised image or two-theta scan, Res 14 (1996) 235–248, https://doi.org/10.1080/08957959608201408.
[35] G.A. Faria, Exploring Metallic Materials Behavior Through in Situ Crystallographic Studies By Synchrotron Radiation, Universidade Estadual de Campinas, 2014. https://bdtd.ibict.br/vufind/Record/CAMP_ef98c2e22e63ff089128f7b4e93e7a3e.
[36] J.D. Escobar, G.A. Faria, L. Wu, J.P. Oliveira, P.R. Mei, A.J. Ramirez, Austenite reversion kinetics and stability during tempering of a Ti-stabilized supermartensitic stainless steel: correlative in situ synchrotron x-ray diffraction and dilatometry, Acta Mater. 138 (2017) 92–99, https://doi.org/10.1016/j.actamat.2017.07.036.
[37] D.J. Dyson, B. Holmes, Effect of alloying additions on the lattice parameter of austenite, J. Iron Steel Inst. 208 (1970) 469–474.
[38] G.R. Lehnhoff, K.O. Findley, B.C. De Cooman, The influence of silicon and aluminum alloying on the lattice parameter and stacking fault energy of austenitic steel, Scr. Mater. 92 (2014) 19–22, https://doi.org/10.1016/j.scriptamat.2014.07.019.
[39] K. Thompson, D. Lawrence, D.J. Larson, J.D. Olson, T.F. Kelly, B. Gorman, In situ site-specific specimen preparation for atom probe tomography, Ultramicroscopy 107 (2007) 131–139, https://doi.org/10.1016/j.ultramic.2006.06.008.
[40] B. Geiser, D. Larson, E. Oltman, S. Gerstl, D. Reinhard, T. Kelly, T. Prosa, Wide-field-of-view atom probe reconstruction, Microsc. Microanal. 15 (2009) 292–293, https://doi.org/10.1017/S1431927609098249.
[41] L. Cheng, C.M. Brakman, B.M. Korevaar, E.J. Mittemeijer, Tempering of iron-carbon martensite; dilatometric and calorimetric analysis, Metall. Trans. A, Phys. Metall. Mater. Sci. 19 A (1988) 2415–2426, https://doi.org/10.1007/BF02645469.
[42] P.M. Group, M. Division, Martensiti c Transformatio n Zenji Nishiyama, 1 st. ed., Kawasaki, 1972.
[43] G.R. Speich, W.C. Leslie, Tempering of Steel, Met. Trans. 3 (1972) 1043–1054, https://doi.org/10.1007/BF02642436.
[44] M.J. Santofimia, L. Zhao, J. Sietsma, Volume change associated to carbon partitioning from martensite to austenite, Mater. Sci. Forum. 706–709 (2012) 2290–2295, https://doi.org/10.4028/www.scientific.net/MSF.706-709.2290.
[45] Z. Wang, M.X. Huang, Optimising the strength-ductility-toughness combination in ultra-high strength quenching and partitioning steels by tailoring martensite matrix and retained austenite, Int. J. Plast. 134 (2020), 102851, https://doi.org/10.1016/j.ijplas.2020.102851.
[46] D. Foster, M. Paladugu, J. Hughes, M. Kapousidou, U. Islam, A. Stark, N. Schell, E. Jimenez-Melero, In-situ synchrotron X-ray diffraction during quenching and tempering of SAE 52100 steel, Mater. Today Commun. 29 (2021), 102930, https://doi.org/10.1016/j.mtcomm.2021.102930.
[47] M. Jung, S.-J. Lee, Y.-K. Lee, Microstructural and dilatational changes during tempering and tempering kinetics in martensitic medium-carbon steel, Metall. Mater. Trans. A. 40 (2009) 551–559, https://doi.org/10.1007/s11661-008-9756-2.
[48] L. Cheng, A. Böttger, T.H. de Keijser, E.J. Mittemeijer, Lattice parameters of iron-carbon and iron-nitrogen martensites and austenites, Scr. Metall. Mater. 24 (1990) 509–514, https://doi.org/10.1016/0956-716X(90)90192-J.
[49] J. Epp, Investigation of triaxial stress state in retained austenite during quenching of a low alloy steel by in situ X-ray diffraction, Adv. Mater. Res. 996 (2014) 525–531, https://doi.org/10.4028/www.scientific.net/AMR.996.525.
[50] S.S. Babu, K. Hono, T. Sakurai, APFIM studies on martensite tempering of Fe-C-Si-Mn low alloy steel, Appl. Surf. Sci. 67 (1993) 321–327, https://doi.org/10.1016/0169-4332(93)90333-7.
[51] F.G. Caballero, M.K. Miller, C. Garcia-Mateo, C. Capdevila, S.S. Babu, Redistribution of alloying elements during tempering of a nanocrystalline steel, Acta Mater. 56 (2008) 188–199, https://doi.org/10.1016/j.actamat.2007.09.018.